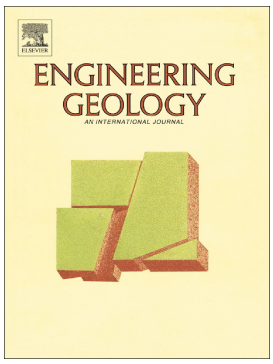

Numerical and theoretical study of bi-planar failure in footwall slopes

Chaoyi Sun, Congxin Chen, Yun Zheng, Wei Zhang, Feng Liu

PII: S0013-7952(19)30432-6
DOI: https://doi.org/10.1016/j.enggeo.2019.105234
Article Number: 105234
Reference: ENGEO 105234

To appear in: *Engineering Geology*

Received date: 11 March 2019
Revised date: 18 July 2019
Accepted date: 19 July 2019

Please cite this article as: C. Sun, C. Chen, Y. Zheng, et al., Numerical and theoretical study of bi-planar failure in footwall slopes, Engineering Geology, https://doi.org/10.1016/j.enggeo.2019.105234

Numerical and theoretical study of bi-planar failure in footwall slopes

Chaoyi Sun[1,2], Congxin Chen[1], Yun Zheng[1,*] yzheng@whrsm.ac.cn, Wei Zhang[1], Feng Liu[3]

[1]*State Key Laboratory of Geomechanics and Geotechnical Engineering, Institute of Rock and Soil Mechanics, Chinese Academy of Sciences, Wuhan, Hubei 430071, China*

[2]*University of Chinese Academy of Sciences, Beijing 100049, China*

[3]*School of Civil Engineering, Tianjin University, Tianjin, 300072, China*

[*]Corresponding author.

Abstract

Bi-planar failure is the commonest type of failure in steep and high footwall slopes. This paper presents an investigation of the bi-planar failure mechanism and a stability analysis model for footwall slopes based on the study of eleven diabase mines in Hunyuan County, Shanxi Province, China. First, a detailed investigation of the site and tests were carried out to obtain a geological model and calculation parameters for the slope. Then, the failure process in footwall slopes was investigated by a trigon approach performed using the Universal Distinct Element Code (UDEC) software package. A mechanism was then obtained for bi-planar compression–shear failure by combining the results obtained for the stress, displacement, and crack development. Subsequently, based on the limit equilibrium and frictional plasticity theories, a new columnar mechanical model was proposed for bi-planar footwall slope failure. The results demonstrate that the UDEC trigon approach was well suited to simulating bi-planar failure in steep and high footwall slopes. Employing this approach, a sliding failure surface that initiates, develops, and propagates in the discontinuity and intact rock could be correctly captured and the evolution of the damage in the toe of the slope could be quantitatively investigated. The results also indicate that shear failure first occurs at persistent discontinuities and then

compression–shear failure occurs in the intact rocks. In addition, the failure surface of the rock emanates from the toe of the slope, is oriented upwards at an angle to the persistent discontinuity thus forming the through sliding surface (this angle can be determined using frictional plasticity theory). The critical heights and safety factors of footwall slopes could be readily obtained by employing this new columnar mechanical model giving results that are consistent with the results of numerical simulations. Furthermore, the results of a parameter-sensitivity analysis show that the dip angle of the toe breakout surface increases as the slope angle increases. However, the angle between the toe breakout and internal shear surfaces remains unchanged as the slope angle increases. Moreover, the critical height of the footwall slope decreases linearly as the slope angle increases. The method proposed provides theoretical guidance for the stability analysis of steep and high footwall slopes. The results produced should also help engineers to gain a better understanding of the mechanisms of bi-planar failure in such rock slopes.

Keywords: Footwall slope; bi-planar failure; UDEC trigon approach; slope stability analysis; limit equilibrium method.

1. Introduction

In surface mining where the strata have been subjected to tectonic folding, slopes are often excavated parallel to the dip of the strata to reduce costs. This can generate extensive footwall slopes that are steep, high, and unbenched (Stead and Eberhardt, 1997). In such cases, slope instability is often structurally controlled by, for example, joint sets, faults, or weak zones parallel or sub-parallel to the slope (Calder and Blackwell, 1980; Alejano et al., 2001; Fisher, 2009; Alejano et al., 2011; Yin et al.,

2011; Tanyas et al., 2013; Havaej et al., 2014). Furthermore, any subsequent failure can be generally divided into one of three types: bi-planar, ploughing, and buckling (Stead and Eberhardt, 1997; Fisher, 2009; Alejano and Juncal, 2010; Alejano et al., 2011; Havaej et al., 2014). Of these, the most common type is bi-planar failure that may be fully or partially controlled by discontinuities.

If the bi-planar failure is fully joint-controlled, then the stability is primarily governed by the strength of the pre-existing discontinuities. In the partially-controlled case (i.e. where there is an absence of crosscutting structures near the toe of the slope), the bi-planar failure can be more complex. Thus, sliding may occur along the major geological discontinuities, causing compression and shearing of the intact rock. In such circumstances, a detailed investigation of the precise nature of the failure mechanism and a stability analysis are necessary.

Stead and Eberhardt (1997) have reviewed the key factors affecting the stability of footwall slopes in surface coal mines. They summarized the main failure mechanisms in such slopes and introduced the use of numerical simulations to analyze the various failure mechanisms. Alejano and Alonso (2005) described the main failure modes for footwall slopes and obtained the safety factors of such slopes using the shear and tensile strength reduction technique. Fisher and Eberhardt (2007) proposed some practical recommendations to help evaluate the stability of footwall slopes based on discrete element simulation together with limit equilibrium analysis. Alejano et al. (2011) carried out a comparative analysis of footwall slopes using theoretical methods, numerical simulations, and physical models and thus obtained safety factors for slopes susceptible to bi-planar failure. Ning et al. (2011) employed a numerical manifold method to analyze the potential failure mechanisms of footwall slopes and discussed the various failure modes for persistent discontinuities and crosscutting joints with different dip angles. Havaej et al. (2014) also investigated bi-planar footwall slope failure and identified three

vital failure surfaces associated with such failure that relate to the persistent discontinuity, the toe breakout surface, and the internal shear surface.

The abovementioned research has made a valuable contribution to the study of bi-planar footwall slope failure. These footwall slopes are not very steep with slope angles in the range 30–60°. However, in Hunyuan County, Shanxi Province, in China (Fig. 1), where there are eleven diabase mines, the footwall slopes subjected to strong tectonic deformations have slope angles that vary from the 60° to 75° (according to site investigations and statistical analyses). Thus, these diabase mines have slopes that are much steeper than those generally found elsewhere (Stead and Eberhardt, 1997; Alejano et al., 2011; Havaej et al., 2014). Furthermore, these footwall slopes are often very high: up to 150 – 210 m. Not many similar cases associated with such steep and high footwall slopes have been reported.

In this paper, we focus on the abovementioned diabase mines in Hunyuan County and propose a novel model to evaluate the stability of these kinds of footwall slope. First, we reported the results of a detailed site investigation and other tests carried out to allow us to derive a geological model for the slope and other calculation parameters. Then, the failure process in the footwall slope was investigated by combining analysis results obtained for stress, displacement, and crack development. A trigon approach was adopted using Universal Distinct Element Code (UDEC). We thus identified the mechanism responsible for bi-planar compression–shear failure of the footwall slopes. Based on limit equilibrium and frictional plasticity theories, a new columnar mechanical model for bi-planar footwall slope failure was proposed. Finally, a comparison was made of results obtained using the proposed method and by numerical simulation. Good agreement was found which indicates that the columnar model can delineate the bi-planar failure of such steep and high footwall slopes both accurately and quickly.

2. Engineering geology and rock mass parameters

2.1 Geological environment

The diabase mines in Hunyuan County are situated in a mountainous area. They thus encounter steep terrain and cut deep into the valley. The mountain is mostly composed of ancient gneiss that has suffered strong weathering and denudation. After different stages of long-term tectonic movement, a set of geologic bodies have been formed that show signs of migmatization. They are mixed with a large number of ancient intrusive rock masses, forming a large-scale diabase deposit (Chen et al., 2017). Subsequent mining of the deposits has been performed via a sequence of excavations parallel to the dip of the strata. As a result, steep and high footwall slopes have been generated.

The lithology and hydrogeological conditions of the footwall slopes have been analyzed based on data obtained by drilling (Chen et al., 2017). The rock surrounding the slope is mainly composed of biotite plagiogneiss according to cores derived from boreholes (see the example presented in Fig. 2). Furthermore, the gneiss rock has been significantly degraded. The gneissosity or foliation is well developed, recrystallization is obvious, mineral particles are coarse, the flaky mineral content is high, and the rock structure has clearly changed.

Based on the site geology and drilling data, the lithology of the footwall slope formation can be divided into two engineering geological layers: (i) Miscellaneous fill and residual soil covering the entire surface of the slope crest to a thickness of 0.5–2.5 m (which is variegated, loose, and slightly wet). (ii) Moderately-weathered biotite plagiogneiss, containing mainly biotite, quartz, and plagioclase with a fine crystalloblastic texture and gneissic structure, as well as grayish white or grayish black

features. Most of the cores consist of short columns that are 10–100 cm long (some pieces are 5–10 cm long). Thus, the rock quality designation (RQD) is about 80 which indicates that the slope rock is of medium quality.

The hydrogeological conditions in the mining area are relatively simple. The groundwater present is classed as phreatic bedrock fissure water as it is deeply buried and surface water is not well developed. The fissure water is mainly supplied by meteoric water penetrating along the interbedded fissures, for example, joint sets, faults, or weak zones. At the same time, small-scale perched water may be generated by meteoric water penetrating the cracks in the rock. Furthermore, diabase with its dense rock structure is an aquifuge and gneiss lacking developed cracks has a poor water-retaining capacity. In addition, the groundwater supply is rather limited as there is not enough meteoric water or perennial surface runoff. Therefore, the groundwater in the footwall slope area is of the deeply-buried type.

2.2 Rock mass structure

The footwall slope is low in the south and high in the north with a slope height of 150–210 m. The slope stratum is monoclinic and the average orientation of the slope is 68°∠ 70° (i.e., the average dip and dip direction are 68° and 70°, respectively) (Fig. 1b). Three joint sets (J1–J3) are found in the slope region from an investigation of the geological outcrops and digital borehole camera images, as shown in Fig. 3.

The first joint set, J1, has an orientation of 75°∠ 70°, a NEE dipping direction. It has high persistence with spacing of about 1000 mm. The joint surfaces are smooth and planar in brown, and contain no infilling. This is actually a set of structural planes that are nearly parallel to the schistosity of the rock mass, so it is simply referred to here as the ‘persistent discontinuity’ dipping in the direction of

the slope surface. The second joint set, J2, has an orientation of 161°∠ 82°, a NNW dipping direction. It shows medium persistence with spacing of about 500 mm. The joint surfaces are smooth and undulating in maroon, and contain no infilling. This set of structural planes is nearly perpendicular to the dipping direction of the slope surface. Finally, the third joint set, J3, has an orientation of 342°∠ 66°, a SSE dipping direction, and spacing of about 650 mm. The joint is generally partly open and has low-to-very low persistence. This set of structural planes is also nearly perpendicular to the dipping direction of the slope surface. A pole plot of the discontinuous structural planes and slope surface is shown in Fig. 4. The rock mass cut by these three sets of structural planes thus has a block-layered structure with poor integrity.

From the perspective of formation lithology, the miscellaneous fill and residual soil layers are so thin that their effect on the geological model can be ignored. Consequently, the subsequent analysis is simplified by only considering the moderately-weathered gneiss in the geological model. In addition, from the perspective of rock mass structure, only the persistent discontinuity (J1) belongs to the geological profile of the footwall slope, as shown in Fig. 5. Thus, J1 plays an important role in the two-dimensional slope stability analysis.

2.3 Rock mass parameters

The discontinuities in the rock mass (e.g. joints, cracks, and bedding planes) cause the macroscopic mechanical properties to be degraded. As a result, the strength and deformation modulus of the rock mass are much smaller than those of intact rock. Therefore, it is necessary to 'calibrate' the rock mass parameters (Brady and Brown, 2006).

Many different rock mass classification systems have been established to indicate the quality of

the rock. Examples include the RQD, rock mass rating (RMR), geological strength index (GSI), basic quality index (BQ), and tunneling quality index (Q) systems. The RQD system is a simple, efficient, and practical system to use. Furthermore, Zhang and Einstein (2004) established an empirical relationship connecting the deformation moduli of the rock mass, E_m, and intact rock, E_r, in terms of the RQD, namely,

$$E_m = E_r \cdot 10^{0.0186RQD - 1.91}. \quad (1)$$

Based on many laboratory tests on small specimens (50 × 100 mm) following standards recommended by the International Society for Rock Mechanics (ISRM) (Fairhurst and Hudson, 1999), the mean deformation modulus of the intact gneiss rock was determined to be 33 GPa. Combining this with a mean RQD of 80 and using Eq. (1) gives a value of 12.5 GPa for the deformation modulus of the rock mass.

The Mohr–Coulomb strength parameters of the rock mass could be calculated using the Hoek–Brown failure criterion (Hoek et al., 2002). More specifically, the cohesion (c_r) and friction angle (φ_r) of the rock mass were obtained by linearly fitting the nonlinear Hoek–Brown strength parameters using RocLab software. The calculation involves four basic parameters: the uniaxial compressive strength of the intact rock (σ_{ci}), the GSI value, the Hoek–Brown constant (m_i), and the disturbance factor of the rock mass (D). First, the mean uniaxial compressive strength of the intact gneiss rock was obtained via a large amount of uniaxial compression tests which produces a value of 120 MPa. Then, a quantitative GSI chart was used to determine the GSI value (giving a value of 45 considering the rock mass structure and surface conditions encountered). Finally, values were determined for m_i and D according to the lithology and excavation characteristics of the footwall slope. The rock mass strength parameters thus determined are listed in Table 1.

The tensile strength (σ_{tr}) of the rock mass can be obtained from the cohesion (c_r) and friction angle (φ_r) via the Coulomb criterion by using the following equation:

$$\sigma_{tr} = \frac{2c_r \cdot \cos\varphi_r}{1+\sin\varphi_r}. \tag{2}$$

The physical and mechanical parameters of the gneiss rock mass can now be listed, as shown in Table 2.

3. Compression–shear failure mechanism

3.1 The UDEC trigon approach

The discontinuities found in rocks (joints, cracks, bedding planes, etc.) make the application of continuum mechanics very difficult (Yang et al., 2017; Yan and Jiao, 2019; Yan et al., 2019). Discrete-element methods can not only present the broken rock state but also reveal the rock failure process better than their finite-element counterparts. This is because they can simulate the fracture, movement, and large deformations involved. For example, one of the most common discrete-element packages, UDEC, is able to simulate the large movement and deformation of a blocky system very well using a 'Lagrangian' scheme of calculation (Cheng et al, 2018; Huang et al, 2018; Zheng et al., 2019).

Gao (2013) and Gao and Stead (2014) have used UDEC to simulate rock assemblies using trigon blocks. In their work, a single block is regarded as an independent object in the mechanical solution and these are connected by their contact with the blocks surrounding them to allow the failure process and large deformations to be simulated. Compared with the Voronoi blocks that are conventionally used in such work, trigon blocks are less dependent on the computational grid. They are better suited to simulating friction angle and failure mode (Gao, 2013; Gao and Stead, 2014). Gao et al. (2014a, b)

applied this UDEC trigon approach to the study of a coal mine roadway, successfully obtaining the failure mode and collapse mechanism of the roadway roof. More recently, Zheng et al. (2018b) also adopted this approach to investigate flexural toppling failure in anti-inclined rock slopes.

In the UDEC trigon approach, an elastic model is used to describe the mechanical behavior of the trigon blocks and a coulomb slip model is used to describe the contact between them. Thus, rock failure is controlled by the occurrence of contact failure and this may happen if either a shear or tension stress is applied to the contacts that exceeds either the shear or tensile strength, respectively (Itasca, 2014). There are three kinds of mechanical behaviors relating to the contacts. First, when the contact stress between the blocks does not exceed its strength, the model experiences deformation that is controlled by the block deformation modulus and contact stiffness will occur. Second, when the contact shear stress exceeds the shear strength, shear failure of the contacts will occur and the adjacent blocks will slide. Third, when the contact normal stress exceeds the normal strength, tensile failure of the contacts will occur and the adjacent blocks will become detached.

The mechanical properties of the rock mass, such as anisotropy and discontinuity, are defined by the mechanical parameters that are assigned to the blocks and contacts. More specifically, the deformation behavior of the trigon blocks is controlled by the shear (G) and bulk (K) moduli, the deformation behavior of the contacts is controlled by their normal (k_n) and shear (k_s) stiffness, and the strength of the contacts is controlled by their cohesion (c_j), friction angle (φ_j), and tensile strength (σ_{tj}). The following equations are used to calculate some of these parameters (Itasca, 2014; Gao and Stead, 2014; Kazerani & Zhao, 2010):

$$K = \frac{E_m}{3(1-2\mu)} \tag{3}$$

$$G = \frac{E_m}{2(1+\mu)} \tag{4}$$

$$k_n = n\left[\frac{K+(4/3)G}{\Delta z_{\min}}\right], \quad 1 \le n \le 10 \tag{5}$$

$$k_s = k_n\left(\frac{G}{E}\right) \tag{6}$$

where μ is the Poisson's ratio of the rock mass, and $\Delta z_{\min}$ is the smallest width of the zone adjoining the contact in the normal direction.

3.2 Numerical model for the footwall slope

To simulate bi-planar failure, a numerical model for the footwall slope was created based on its geological profile (Fig. 5) using UDEC, as shown in Fig. 6. The model has a width of 400 m and height of 350 m; the slope angle is 70° and the final excavation depth (i.e. slope height) is 225 m. The persistent discontinuity dips in the model at an angle of 70° and spacing of 20 m. A statistical analysis performed by Fisher (2009) showed that the thickness of a bi-planar footwall slope failure (t) is generally less than one-third of the slope height (h), and that the t/h ratio generally decreases as the slope angle increases. In this study, the value of t/h is taken to be 0.09, thus the failure thickness of the footwall slope is calculated to be 20 m. Therefore, the spacing of the persistent discontinuity J1 in the numerical model is taken to be 20 m.

To improve the computational efficiency of the model, only the area of interest was discretized using the UDEC trigon approach. Trigon blocks with an average edge length of 2 and 3 m were thus generated in the lower and upper area of interest, respectively. The horizontal displacement of the model was constrained along its lateral boundaries, and the vertical and horizontal displacements were fixed at the bottom boundary. Finally, stress and displacement monitoring points (M1–M3) were installed at the top, middle, and bottom of the slope surface (see Fig. 6).

3.3 Calibration of the micro-parameters in the UDEC model

The micro-properties of the trigon blocks and contacts control the mechanical response of the rock mass. Therefore, they must be calibrated to ensure the response is realistic. To that end, a series of compression and tensile tests were performed to achieve consistency between the micro-properties of the contacts and macro-properties of the rock mass (Christianson et al., 2006; Gao and Stead, 2014; Mayer and Stead, 2017).

Christianson et al. (2006) recommend that the dimensions of the test samples used should be at least 10 times the size of the internal blocks in order to reduce boundary effects. Thus, rectangular test samples measuring 35×70 m were adopted in this work (as the trigon blocks used have edges of average length 2 and 3 m).

The deformation modulus, Poisson's ratio, and normal and shear stiffness of the block contacts can be obtained by carrying out a series of unconfined compression tests. As for the cohesion and friction angle of the contacts, they can be obtained by conducting a series of confined compression tests. Based on the stress–strain curves generated using different confining pressures, the strength envelope can be obtained from a (linear) regression analysis of the compressive strength for the various confining pressures. Subsequently, the cohesion (c_j) and friction angle (φ_j) of the contacts can be obtained from the gradient (m) and vertical intercept (b) of the strength envelope graph (Kovari et al., 1983):

$$\varphi_j = \arcsin\left(\frac{m-1}{m+1}\right) \tag{7}$$

$$c_j = b\frac{(1-\sin\varphi)}{2\cos\varphi} \tag{8}$$

The tensile strength of the contacts can be acquired by performing a series of tensile tests. Although direct tensile tests are difficult to be realized in the laboratory, the tensile strength can be

quickly and easily obtained via numerical simulation (Shang et al., 2018; Moosavi et al., 2018). Therefore, direct tensile tests were also performed on rectangular 35×70 m samples to obtain the tensile strength of the contacts in this paper.

First, a set of typical values were assumed for the contact micro-parameters. Then, compression and direct tensile tests were conducted iteratively until the simulated test results were consistent with the macro-parameters of the rock mass as listed in Table 2. The deformation and strength characteristics obtained are shown in Fig. 7. For the same macro-parameters of the rock mass, the size of the trigon blocks mainly has a strong influence on the deformation parameters of the contacts but basically no effect on the strength parameters. Finally, the most appropriate micro-parameters for the blocks and contacts in the UDEC trigon model were elucidated, as presented in Table 3.

3.4 Analysis of the failure process

To simulate the footwall slope, the numerical model shown in Fig. 6 was employed together with the model parameters listed in Table 3. We also need mechanical parameters for the persistent discontinuity J1 which can be obtained by conducting a number of laboratory tests (Chen et al., 2017). The laboratory direct shear tests on the discontinuity planes were conducted in accordance with the methods recommended by Muralha et al. (2014) and Meng et al. (2019). The strength parameters of the joints were determined based on laboratory tests and engineering analogy method. Since characterization of the joints (JRC, JCS, Schmidt hammer rebound, etc.) was not obtained during the field investigation, the effect of joint roughness (at field-scale) on strength parameters was not considered in the analysis. Table 4 summarizes all of the joint parameters used in the numerical model.

The footwall slope model was first brought into initial stress equilibrium under gravitational

loading. After this, blocks above the cut slope were deleted to simulate excavation of the slope. If block removal is too sudden, however, the response of the model may be unstable. Such action is also not a realistic portrayal of what happens in the field. Therefore, to model excavation more realistically and also ensure correct solutions were obtained from the model, excavation was carried out gradually and step-by-step calculations were adopted in each excavation stage as the blocks were deleted (Gao et al., 2014a; Gao et al., 2014b; Yang et al., 2019).

The slope model was first excavated to a depth of 150 m along the cut slope boundary. It was then excavated to a depth of 210 m and then to 225 m in 5 m stages. During each excavation stage, step-by-step calculations were used to gradually relax the boundary forces. This was achieved using the modified FISH function 'ZONK.FIS'. This function in UDEC was mainly applied to the excavation of roadways, tunnels, and underground spaces. It can detect the interior boundaries of the excavation and gradually relax the forces on them according to a release factor R which changes from 0 to 1 (for example, an R value of 0.2 indicates that 20% of the force applied to an excavation boundary is released in each relaxation stage, giving a total of 5 relaxation stages). This ensures that a stable response comes from the model. However, the excavation boundaries of slopes are outer boundaries, which is different to the situation encountered when excavating roadways, tunnels, and underground spaces. Thus, the modified FISH function, ZONK.FIS, was developed that detects the outer boundary of the area of interest to achieve a gradual relaxation of the boundary forces on the slope.

Another FISH function, 'damage.fis', was developed to track and record the lengths of the failed contacts in the area of interest based on their shear and tensile failure characteristics. This was used to quantitatively evaluate the failure process in the footwall slope. Furthermore, damage parameters were defined in terms of these failure lengths in the area of interest according to the following equations

(Gao et al., 2014a; Gao et al., 2014b):

$$D_s = \frac{l_s}{l_c} \times 100\% \tag{9}$$

$$D_t = \frac{l_t}{l_c} \times 100\% \tag{10}$$

where D_s (D_t) is the shear (tension) damage parameter, l_s (l_t) represents the shear (tension) failure length, and l_c is the total contact length.

The results of the bi-planar footwall slope failure simulations are illustrated in Figs. 8–11.

Fig. 8 shows the development of cracks caused by the downward excavation of the slope at various stages. As the slope is excavated downwards, the persistent discontinuity first undergoes sliding failure in the first two stages shown (Figs. 8a and 8b). Subsequently, the toe of the slope is squeezed and shear cracks are generated in the toe when the excavation depth reaches 215 m (stage 3; Fig. 8c). Thereafter, the shear cracks extend obliquely upwards. They eventually penetrate the sliding surface of the persistent discontinuity to form a through sliding surface (stage 4; Fig. 8d). Finally, an internal shear surface is generated and there is further sliding (mass deformation) of the footwall slope, leading to kinematic release (stage 5; Fig. 8e). The ultimate distribution of cracks in the footwall slope is shown in Fig. 8e, which indicates that the bi-planar failure process is dominated by shear failure accompanied by sporadic tensile failure.

The development of damage due to shear and tensile failure in the intact rock and persistent discontinuities is illustrated in Fig. 9. For the intact rock, the damage is mainly concentrated in the toe of the slope and the total damage parameter is 4.83% in the ultimate damage state of the trigon model. Moreover, the shear and tension damage parameters are 4.70% and 0.13%, respectively, so that these damage modes account for 97.36% and 2.64% of the total contact damage, respectively (Fig. 9a).

In contrast, almost all of the damages associated with the failure of the persistent discontinuities

occur above the toe of the slope in the ultimate damage state of the trigon model. The total damage parameter is 85.16% with shear damage accounting for 100% of the total contact damage (Fig. 9b).

Fig. 9 shows that, overall, from the perspective of damage development, the failure of the persistent discontinuity precedes that of the intact rock. Put more formally, it depicts a progressive failure process in which the shear failure of the persistent discontinuity occurs first and this subsequently damages the intact rock.

Fig. 10 illustrates the progressive failure of the footwall slope from the perspective of the monitoring points M1–M3. Fig. 10a shows the variation of the horizontal stress experienced by the monitoring points during excavation as well as the five stages indicated in Fig. 8. At stage 1 (excavation depth of 150 m), the horizontal stresses at points M1 and M3 are decreasing in a stepwise manner, mainly due to the effect of excavation and unloading. In contrast, the horizontal stress at M2 increases at first and then decreases. This is because M2 is located at the toe of the slope after the first stage of slope excavation. Stress concentration in the toe of the slope causes the internal stress to increase, and then the secondary adjustment of the stress causes the internal stress to decrease. Moreover, the five steps in the curve presented in this one excavation stage are consistent with the calculation of the five force-relaxation stages according to the modified FISH function ZONK.FIS.

At stage 2 (excavation depth of 210 m), the horizontal stress at M1 remains basically unchanged and is approximately zero. The horizontal stress at M2 decreases stepwise (mainly due to the effect of excavation and unloading). The horizontal stress at M3 increases stepwise at first and then decreases, which is also because M3 becomes located at the toe of the slope after the second stage of slope excavation.

At stage 3 (excavation depth of 215 m), the horizontal stresses at M1 and M2 basically remain

unchanged, which is essentially because the excavation face is far away from M1 and M2. The horizontal stress at M3 decreases stepwise. This is because the shear cracks near the toe of the slope cause horizontal stress to be released.

At stages 4 and 5 (excavation depth of 215 m), the horizontal stresses at M1, M2, and M3 all decrease to approximately zero. This is because the toe breakout surface penetrates the sliding surface of the persistent discontinuity to produce bi-planar failure (which leads to stress release).

The corresponding displacements of the monitoring points are shown in Fig. 10b. In the first three stages, the displacements of the points all increase slowly. This is mainly due to the absence of a through sliding surface. When stage 4 is reached, the toe breakout surface penetrates the sliding surface of the persistent discontinuity to generate the bi-planar sliding mass. Subsequently, the deformation of the sliding mass increases rapidly so that the displacements of the points rapidly increase. At this stage, the large deformation of the sliding mass causes the compression–shear failure of the toe of the slope to be further aggravated, and a large amount of damage occurs in the rock. This is, of course, highly consistent with the damage shown in Fig. 9a. It also indicates that the compression–shear failure of the rock in the toe of the slope plays a significant role in the bi-planar failure process.

Fig. 11. Principal stress paths associated with five excavation stages for different zones showing: (a) M1, (b) M2, and (c) M3.

Fig. 11 shows the principal stress paths associated with five excavation stages in different zones (M1 to M3): the principal stresses in the three zones all approximately decrease to zero in the ultimate damage state, which indicates that these zones are all in a state of failure. This illustrates that the stress release is induced by the bi-planar failure occurring after footwall slope excavation.

The minimum principal stresses in the three zones almost all decrease upon excavation, mainly

due to the stress release associated therewith. For the maximum principal stress, the situation is more complex: the maximum principal stress on zone M1 located at the top of the slope surface decreases to approximately zero, due to the effects of excavation and unloading. The maximum principal stress on zone M2 located at an excavation depth of 150 m first increases, then decreases. This is because zone M2 is located at the toe of the slope after the first stage of slope excavation. Stress concentration in the toe of the slope causes the internal stress to increase, and then the subsequent excavation causes the internal stress to decrease. Similarly, the maximum principal stress on zone M3 decreases at first, mainly due to the stress release of first stage of slope excavation. Then, the maximum principal stress on zone M3 increases on account of the stress concentration in the toe of the slope during the second stage of slope excavation. Next, the decrease in the maximum principal stress on zone M3 is due to subsequent slope excavation. This reveals that the changing stress-path induced by slope excavation is an underlying factor controlling bi-planar footwall slope failure.

Fig. 12 shows the ultimate damage state of the footwall slope when the excavation depth is 215 m. The figure indicates that the failure process involves three failure surfaces: the persistent discontinuity, toe breakout surface, and internal shear surface. This is consistent with the results simulated using a model with a continuous material (Fisher and Eberhardt, 2007; Fisher, 2009; Alejano et al., 2011). In other words, the mechanism of bi-planar failure can be captured by both conventional UDEC and Trigon models. The former can be easily used due to the lack of need for micro-parameter calibration and its high computational efficiency, while the latter allows the simulation of intact fracture of blocky media (Gao, 2013; Gao and Stead, 2014). Furthermore, these failure surfaces satisfy the requirements of frictional plasticity theory (Fisher and Eberhardt, 2007), that is:

$$\xi = \varphi_r / 2 + \theta - 45° \tag{11}$$

$$\zeta = \varphi_r + 90° \tag{12}$$

where ξ is the dip angle of the toe breakout surface, φ_r is the friction angle of the rock mass, θ is the dip angle of the persistent discontinuity (i.e. slope angle), and ζ is the angle between the toe breakout and internal shear surfaces.

According to this numerical model, we have $\xi = 46°$ and $\zeta = 137°$ from Fig. 11. In addition, employing frictional plasticity theory, ξ and ζ can be calculated using Eqs (11) and (12) which produces angles of 45° and 131°, respectively. Thus, the results of these two methods of calculation are essentially consistent, which illustrates the feasibility of using the UDEC trigon approach to evaluate the stability of steep and high footwall slopes.

4. Analysis model for bi-planar failure

In this section, we develop a model to allow us to further analyze bi-planar failure in steep and high footwall slopes. When the toe breakout surface penetrates the sliding surface along the persistent discontinuity (Fig. 8d), bi-planar footwall slope failure will occur (Fig. 8e), namely, the slope is in a state of limit equilibrium at that time. In other words, the slope has reached the limit equilibrium state before the subsequent internal shear surface is formed. According to the research above, the failure of the toe of the slope satisfies frictional plasticity theory. The overlying rock slides down the persistent discontinuity to squeeze the rock at the toe of the slope, causing the rock in the toe to undergo compression–shear failure in a similar way to uniaxial compression. Therefore, the sliding mass can be divided into two parts: an upper part that is regarded as the axial load, and a lower part that is regarded as a columnar sample subjected to compression (Fig. 13). The loading surface of the columnar sample, i.e., the boundary between the overburden and columnar sample, is perpendicular to the axial load (the

residual sliding force from the overburden), therefore, the columnar block having a base normal to the main sliding plane rather than the newly formed discontinuity is considered in the analytical model.

4.1 Columnar mechanical model

Fig. 14 shows the resulting columnar model for a steep and high footwall slope subjected to bi-planar failure. The method of analysis is based on the assumption that the principal stress direction of the bi-planar sliding mass is parallel to the slope direction. That is, only the axial load of the overburden on the rock of the toe of the slope is considered. Thus, the angle between the toe breakout surface and the perpendicular plane to the slope surface, denoted by α, is given by

$$\alpha = \varphi_r / 2 + 45° . \tag{13}$$

Some geometrical relationships for the columnar model can easily be obtained from Fig. 14a, as follows,

$$h_1 = h_{cr} - t \sin\theta \tan\alpha \tag{14}$$

$$l_1 = \frac{h_1}{\sin\theta} + \frac{t}{\tan\theta} \tag{15}$$

$$l_r = \frac{t}{\cos\alpha} \tag{16}$$

where h_1 is the height of the overburden, h_{cr} represents the critical height of the bi-planar failure, t is the bi-planar failure thickness, l_1 is the slip surface length of the overburden, and l_r is the length of the toe breakout surface.

The weights of the overburden and compressed column are denoted by w_1 and w_2, respectively, where

$$w_1 = \gamma t \left(\frac{h_1}{\sin\theta} \right) + \frac{1}{2} \gamma t \left(\frac{t}{\tan\theta} \right) \tag{17}$$

$$w_2 = \frac{1}{2}\gamma t\left(t\tan\alpha\right) \tag{18}$$

where γ is the weight per unit area of intact rock.

Fig. 14b shows the corresponding force diagram for the model. Considering the forces acting on the overburden, these forces will be balanced (parallel and perpendicular to the slip surface):

$$F = w_1\sin\theta - S_1 \tag{19}$$

$$N_1 = w_1\cos\theta \tag{20}$$

where F is the axial load of the overburden on the columnar sample, $S_1 = N_1\tan\varphi_j$ is the shear force acting at the slip surface, and N_1 is the normal force acting on the overburden. When analyzing the stability of rock slopes, it is generally assumed that the discontinuities are cohesionless (Goodman and Bray, 1977; Aydan and Kawamoto, 1992, Alejano et al., 2018; Zheng et al., 2018a), and an assumption is also used in this study.

Similarly, balancing the forces acting on the compressed sample column (parallel and perpendicular to the failure surface) yields:

$$w_2\sin\theta + F = N_r\cos\alpha + S_r\sin\alpha \tag{21}$$

$$w_2\cos\theta + S_r\cos\alpha = N_r\sin\alpha \tag{22}$$

where $S_r = N_r\tan\varphi_r + c_r l_r$ and S_r and N_r are the shear and normal forces acting at the shear failure surface of the column sample, respectively.

4.2 Stability analysis

Expressions can be obtained for the critical height and safety factor associated with the bi-planar failure of the footwall slope using the columnar mechanical model and limit equilibrium method. Combining Eqs (19)–(22), we can derive the equation

$$Aw_1 = Bw_2 + C \tag{23}$$

where $A = \sin\theta - \cos\theta \tan\varphi_j$, $B = \dfrac{\cos\theta}{\tan(\alpha - \varphi_r)} - \sin\theta$, and $C = \dfrac{c_r l_r \cos\alpha}{\tan(\alpha - \varphi_r)} + c_r l_r \sin\alpha$.

Introducing Eqs (14)–(18) into Eq. (23) and rearranging yields the following expression for the critical height of the bi-planar footwall slope failure:

$$h_{cr} = \frac{1}{2}\frac{B}{A} t \sin\theta \tan\alpha + \frac{C}{A}\frac{\sin\theta}{\gamma t} + t\left(\sin\theta\tan\alpha - \frac{1}{2}\cos\theta\right) \tag{24}$$

4.3 Comparative analysis

Based on the mechanical parameters for the rock mass and persistent discontinuity derived above (Tables 2–4) and keeping these parameters constant, the stability of the bi-planar footwall slope could be investigated using the newly-proposed and numerical simulation methods. Four values of θ are considered (60°, 65°, 70°, and 75°).

Fig. 15 shows the simulated results for bi-planar failure in these slopes. Each of these slopes presents frictional plasticity failure characteristics and contains three failure surfaces (the persistent discontinuity, toe breakout surface, and internal shear surface). Some of the features of the simulations were further plotted out graphically in Fig. 16 where they were compared with the corresponding results obtained using the theoretical expressions derived here.

Fig. 16a shows the results obtained for the toe breakout angle. The two sets of results are clearly consistent. The percentage errors between the results obtained using the two methods correspond to 7.2%, 6.2%, -1.4%, and -1.2%, as the slope becomes steeper (a mean error of 4.0%). It can also be seen from Fig. 16a that the toe breakout angle increases as the slope angle increases. The results obtained for the angle between the toe breakout and internal shear surfaces, ζ, are also highly consistent (Fig. 16b). The percentage errors in this case amount to 7.2%, 2.1%, -4.6%, and -5.3%, (a mean error of 4.8%).

Fig. 16b also indicates that ζ remains fairly constant as the slope angle increases. In general, these magnitudes of error are very acceptable for both rock mechanics purposes and practical projects. Therefore, it is reasonable to use frictional plasticity theory to study bi-planar failure in such footwall slopes and the results produced are fairly accurate.

Fig. 16c shows a comparison of the results obtained for the critical heights of the bi-planar failure process in the different slopes. Both methods clearly indicate that the critical height decreases linearly as the slope becomes steeper. The results obtained using the two methods are again consistent; overall, however, the value calculated using the theoretical method is generally slightly lower than that derived from the numerical simulation. This is because the theoretical model only considers the axial load of the overburden on the rock in the toe of the slope. However, the direction of principal stress in the sliding mass is not completely parallel to the direction of the slope surface in practice. Only the principal stress direction at the surface of the sliding mass is parallel to the slope direction; the direction of the principal stress will be biased towards the direction of the gravitational force in the deeper parts of the sliding mass. Hence, the axial load acting on the toe of the slope is slightly smaller than the theoretical value. Moreover, the post-failure behavior of rock is considered in the numerical model. It can be seen from Fig. 7b that the post-failure behavior of rock evolves from brittleness in unconfined conditions to strain hardening in the confined (2 MPa) case. This is another reason why the numerical simulation results are not completely consistent with the theoretical results (Figs 15 and 16). Nonetheless, this assumption provides a useful safety margin in practical engineering applications. The percentage errors in the critical height values are -4.6%, -2.5%, -2.3%, and -2.1%, respectively, as the slope angle increases (with a mean 2.9%). The error between the two sets of results is small enough to be acceptable for both rock mechanics and practical applications. This verifies the rationality and

accuracy of the proposed theoretical method of analyzing bi-planar failure in footwall slopes.

5. Conclusions

The work presented here is based on the study of eleven diabase mines in Hunyuan County in China. These mines have steep and high footwall slopes that are subject to bi-planar failure. The compression–shear failure mechanism underlying such failure was investigated in this research via a combination of methods: geological survey, laboratory testing, and modeling using a UDEC trigon approach. To quantitatively evaluate this kind of slope failure, a new theoretical analysis model was subsequently proposed. The key results of the study can be summarized as follows:

(1) The UDEC trigon approach was ideally suited to simulating the bi-planar failure process in steep and high footwall slopes. Using this approach, the sliding failure surface that initiates, develops, and propagates in the discontinuity and intact rock could be correctly captured. Moreover, the evolution of the damage process could be quantitatively investigated in the toe of the slope.

(2) In bi-planar footwall slope failure, the persistent discontinuity undergoes shear failure first. Subsequently, compression–shear failure of the intact rock occurs. The rock failure surface emanates from the toe of the slope and is oriented at an upward angle to the persistent discontinuity thus forming the through sliding surface. This angle could be determined using frictional plasticity theory.

(3) A new columnar model was proposed for bi-planar footwall slope failure based on limit equilibrium and frictional plasticity theory. The critical height and safety factor of the footwall slope could be obtained using this model, giving results that are consistent with those obtained via numerical simulation. Furthermore, the model is better for conducting parameter sensitivity

studies, inversion and reliability analyses, etc.

(4) The dip angle of the toe breakout surface increases as the slope becomes steeper. However, the angle between the toe breakout and internal shear surfaces essentially remains unchanged as the slope angle increases. Moreover, the critical height of the footwall slope decreases linearly as the slope becomes steeper.

Acknowledgments

We would like to acknowledge the reviewers and the editor for their valuable comments and suggestions. This paper was financially supported by the National Natural Science Foundation of China (Grant Nos. 11602284 and 41807280) and Nature Science Foundation of Hubei Province (Grant No. 2018CFB450).

References

Alejano, L.R., Alonso, E. (2005). Application of the 'shear and tensile strength reduction technique' to obtain factors of safety of toppling and footwall rock slopes. Impact of Human Activity on the Geological Environment - Proceedings of the International Symposium of the International Society for Rock Mechanics, Eurock 2005, pp. 7-13.

Alejano, L. R., Ferrero, A. M., Ramírez-Oyanguren, P., & Álvarez Fernández, M.I. (2011). Comparison of limit-equilibrium, numerical and physical models of wall slope stability. International Journal of Rock Mechanics & Mining Sciences, 48(1), 16-26.

Alejano, L. R., García-Bastante, F., Alonso, E., & Gómez-Márquez, I. (2001). Stability analysis and

design of two quarry slopes with the help of numerical modeling. In Proc. of the ISRM Regional Symposium EUROCK 2001, pp. 801-806. Balkema.

Alejano L. R., & Juncal A. S. (2010). Stability analyses of footwall slopes in open pit mining. Dyna, 77(161), 61-70.

Alejano, L. R. , Sánchez–Alonso, C., Pérez–Rey, I., Arzúa, J., Alonso, E. , González, J., Beltramone, L., & Ferrero, A. M. (2018). Block toppling stability in the case of rock blocks with rounded edges. Engineering Geology, 234, 192-203.

Aydan, Ö., & Kawamoto, T. (1992). The stability of slopes and underground openings against flexural toppling and their stabilisation. Rock Mechanics and Rock Engineering, 25(3), 143-165.

Brady, B.H.G., Brown, E.T. (2006). Rock Mechanics for Underground Mining. 3rd ed. Springer Science and Business Media, New York, NY, USA.

Calder, P.N., and Blackwell, G.H. (1980). Investigation of a complex rock displacement at Brenda Mines. The Canadian Mining and Metallurgy Bulletin. August: pp. 1-10.

Chen, C.X., Lu, Z.D., Zheng, Y., & Sun, C.Y. (2017). Reports on the stability evaluation of Juxin and Huabei diabase mine slopes. Institute of Rock and Soil Mechanics, Chinese Academy of Sciences, Wuhan, China (in Chinese).

Cheng, GW, Chen CX, Li LC, Zhu WC, Yang TH, Dai F, & Ren B. (2018). Numerical modelling of strata movement at footwall induced by underground mining. International Journal of Rock Mechanics & Mining Sciences, 108, 142-156.

Christianson, M., Board, M., & Rigby, D. (2006). UDEC simulation of triaxial testing of lithophysal tuff. In: The 41st US Symposium on Rock Mechanics (USRMS). American Rock Mechanics Association.

Fisher, B.R. (2009). Improved Characterization and Analysis of Bi-Planar Dip Slope Failures to Limit Model and Parameter Uncertainty in the Determination of Setback Distances. PhD Thesis The University of British Columbia, Vancouver, Canada.

Fisher, B.R., & Eberhardt, E. (2007). Dip slope analysis and parameter uncertainty, a case history and practical recommendations. In: Eberhardt, Erik, Stead, D., Morrison, T. (Eds.), Rock Mechanics: Meeting Society's Challenges and Demands. Taylor & Francis, pp. 871–878.

Fairhurst, C.E., & Hudson, J.A. (1999). Draft ISRM suggested method for the complete stress-strain curve for the intact rock in uniaxial compression. International Journal of Rock Mechanics & Mining Sciences, 36 (3), 279–289.

Gao F. (2013). Simulation of failure mechanics around underground coal mine openings using discrete element modeling. PhD Thesis. Burnaby: Simon Fraser University.

Gao, F. Q., & Stead, D. (2014). The application of a modified Voronoi logic to brittle fracture modelling at the laboratory and field scale. International Journal of Rock Mechanics & Mining Sciences, 68, 1-14.

Gao, F., Stead, D., & Coggan, J. (2014a). Evaluation of coal longwall caving characteristics using an innovative UDEC Trigon approach. Computers and Geotechnics, 55, 448-460.

Gao, F., Stead, D., & Kang, H. (2014b). Simulation of roof shear failure in coal mine roadways using an innovative UDEC Trigon approach. Computers and Geotechnics, 61, 33-41.

Goodman, R.E., Bray, J.W. (1977). Toppling of rock slopes. In: Rock Engineering for Foundations & Slopes. ASCE, pp. 201–234.

Havaej, M., Stead, D., Eberhardt, E., & Fisher, B. R. (2014). Characterization of bi-planar and ploughing failure mechanisms in footwall slopes using numerical modelling. Engineering Geology,

178(16), 109-120.

Hoek, E., Carranza-Torres, C.T., Corkum, B. (2002). Hoek–Brown Failure Criterion–2002 Edition. Proceedings of the Fifth north American Rock Mechanics Symposium, Toronto, Canada 1, pp. 267–273.

Huang, D., Gu, D. M., Song, Y. X., Cen, D. F., & Zeng, B. (2018). Towards a complete understanding of the triggering mechanism of a large reactivated landslide in the three gorges reservoir. Engineering Geology, 238, 36-51.

Itasca Consulting Group Inc. (2014). UDEC (Universal Distinct Element Code). Version 6.00.282. Software. Minneapolis.

Kazerani, T., & Zhao, J. (2010). Micromechanical parameters in bonded particle method for modelling of brittle material failure. International journal for numerical and analytical methods in geomechanics, 34(18), 1877-1895.

Kovari K., Tisa A., Einstein H., Franklin J. (1983). Suggested methods for determining the strength of rock materials in triaxial compression: revised version. Int J Rock Mech Min Sci Geomech Abstr, 20, 285–290.

Mayer, J. M., & Stead, D. (2017). Exploration into the causes of uncertainty in UDEC grain boundary models. Computers and Geotechnics, 82, 110-123.

Meng, F., Wong, L. N. Y., Zhou, H., Yu, J., & Cheng, G. (2019). Shear Rate Effects on the Post-peak Shear Behaviour and Acoustic Emission Characteristics of Artificially Split Granite Joints. Rock Mechanics and Rock Engineering, 1-20.

Moosavi, S., Scholtès, L., & Giot, R. (2018). Influence of stress induced microcracks on the tensile fracture behavior of rocks. Computers and Geotechnics, 104, 81-95.

Muralha, J., Grasselli, G., Tatone, B., Blümel, M., Chryssanthakis, P., & Yujing, J. (2014). ISRM suggested method for laboratory determination of the shear strength of rock joints: revised version. Rock Mechanics and Rock Engineering, 47, 291-302.

Ning, Y. J., An, X. M., & Ma, G. W. (2011). Footwall slope stability analysis with the numerical manifold method. International Journal of Rock Mechanics & Mining Sciences, 48(6), 964-975.

Shang, J., Duan, K., Gui, Y., Handley, K., & Zhao, Z. (2018). Numerical investigation of the direct tensile behaviour of laminated and transversely isotropic rocks containing incipient bedding planes with different strengths. Computers and Geotechnics, 104, 373-388.

Stead, D., & Eberhardt, E. (1997). Developments in the analysis of footwall slopes in surface coal mining. Engineering Geology, 46(1), 41-61.

Tanyas, H., & Ulusay, R. (2013). Assessment of structurally-controlled slope failure mechanisms and remedial design considerations at a feldspar open pit mine, western turkey. Engineering Geology, 155, 54-68.

Yan, C., & Jiao, Y. Y. (2019). FDEM‐TH3D: A three‐dimensional coupled hydrothermal model for fractured rock. International Journal for Numerical and Analytical Methods in Geomechanics, 43(1), 415-440.

Yan, C., Jiao, Y. Y., & Yang, S. (2019). A 2D coupled hydro-thermal model for the combined finite-discrete element method. Acta Geotechnica, 14(2), 403-416.

Yang, S. Q., Chen, M., Jing, H. W., Chen, K. F., & Meng, B. (2017). A case study on large deformation failure mechanism of deep soft rock roadway in Xin'An coal mine, China. Engineering geology, 217, 89-101.

Yang, Y., Sun, G., Zheng, H., & Qi, Y. (2019). Investigation of the sequential excavation of a

soil-rock-mixture slope using the numerical manifold method. Engineering Geology, 256, 93-109.

Yin, Y., Sun, P., Zhang, M., & Li, B. (2011). Mechanism on apparent dip sliding of oblique inclined bedding rockslide at jiweishan, chongqing, china. Landslides, 8(1), 49-65.

Zhang, L. Y., & Einstein H.H. (2004). Using RQD to estimate the deformation modulus of rock masses. International Journal of Rock Mechanics & Mining Sciences, 41(2), 337-341.

Zheng, Y., Chen, C., Liu, T., Xia, K., & Liu, X. (2018a). Stability analysis of rock slopes against sliding or flexural-toppling failure. Bulletin of Engineering Geology and the Environment, 77: 1383-1403.

Zheng, Y., Chen, C., Liu, T., Zhang, H., Xia, K., & Liu, F. (2018b). Study on the mechanisms of flexural toppling failure in anti-inclined rock slopes using numerical and limit equilibrium models. Engineering Geology, 237, 116-128.

Zheng Y, Chen CX, Liu TT, Song DR & Meng F. (2019). Stability analysis of anti-dip bedding rock slopes locally reinforced by rock bolts. Engineering Geology, 251, 228-240.

Figures

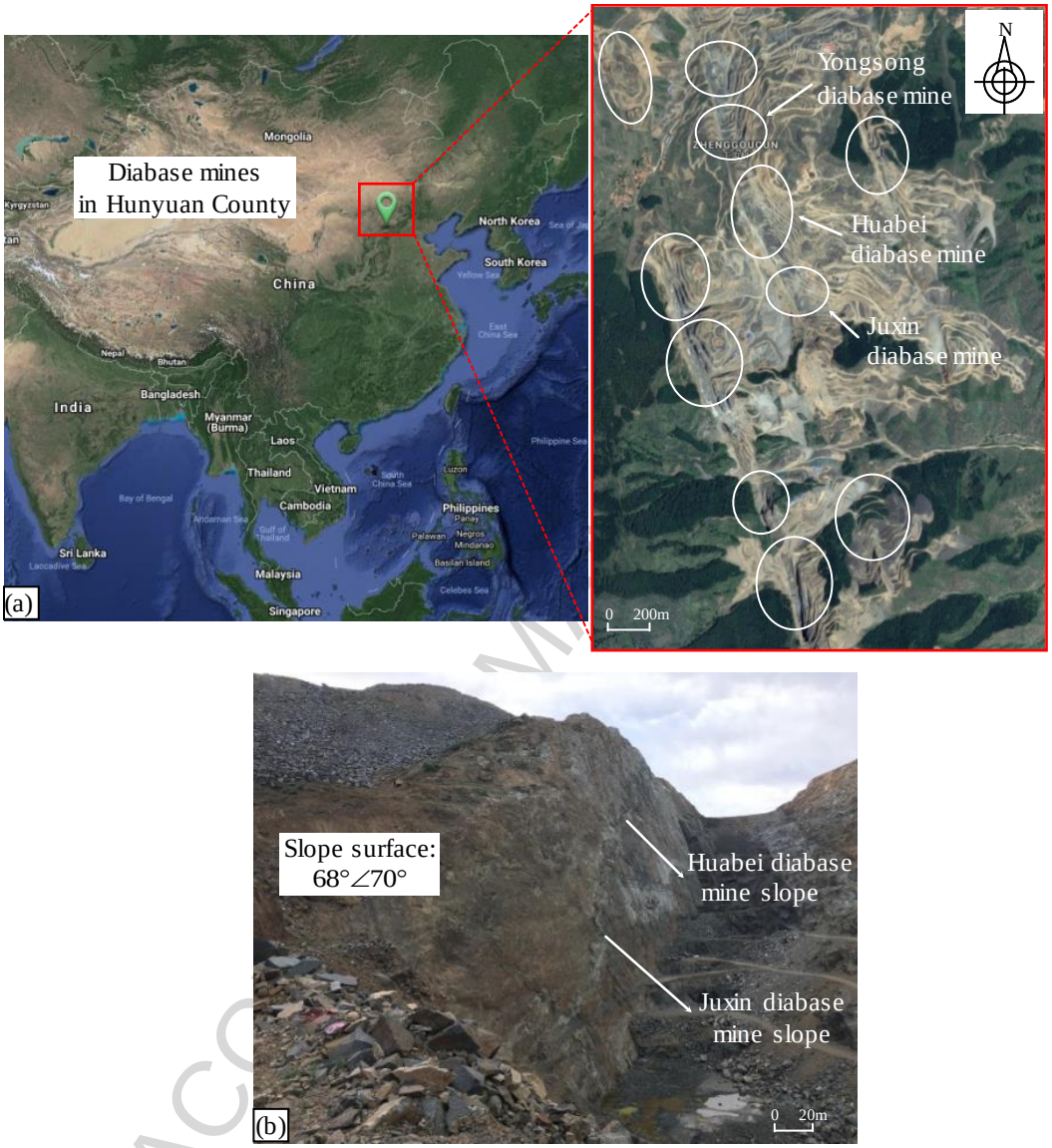

Fig. 1. Details of the diabase mines showing: (a) their location in Hunyuan County, Shanxi, in China (where the white ellipses denote the mines), and (b) a view of the footwall slopes of the Juxin and Huabei diabase mines.

Fig. 2. Photograph of the borehole core from the 2nd borehole.

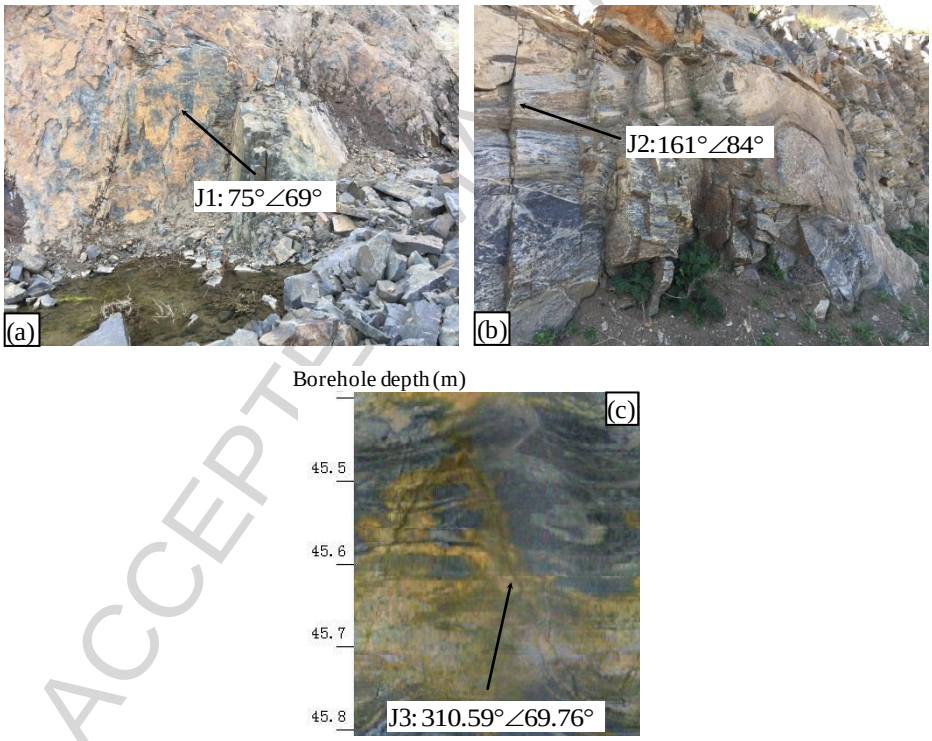

Fig. 3. The three preferred structure planes derived from an inspection of the geologic outcrops and borehole camera images showing: (a) J1, (b) J2, and (c) J3.

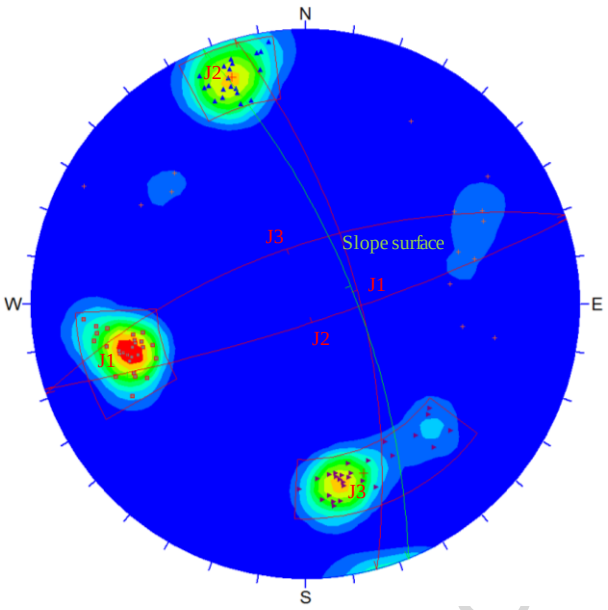

Fig. 4. Pole plot of the discontinuous structural planes.

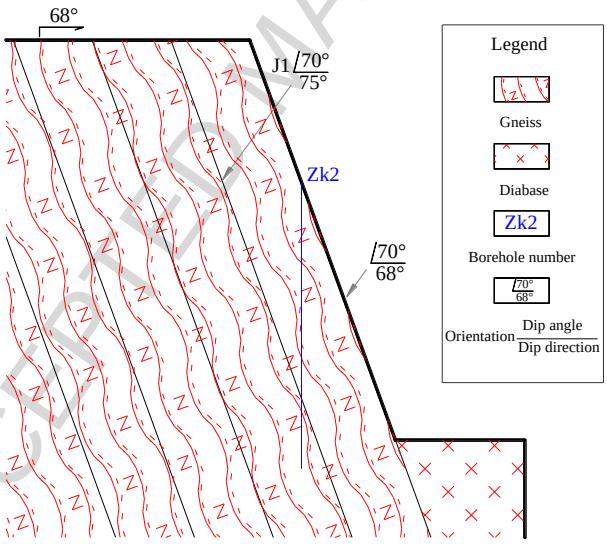

Fig. 5. Geological profile of the footwall slope.

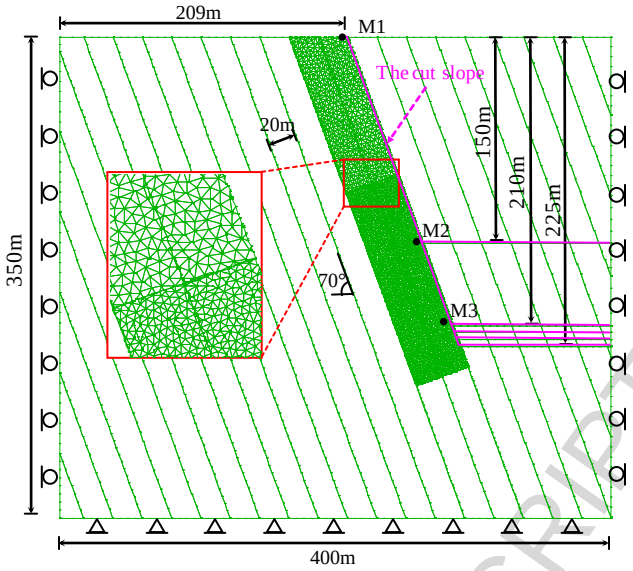

Fig. 6. Numerical model for the footwall slope built using UDEC.

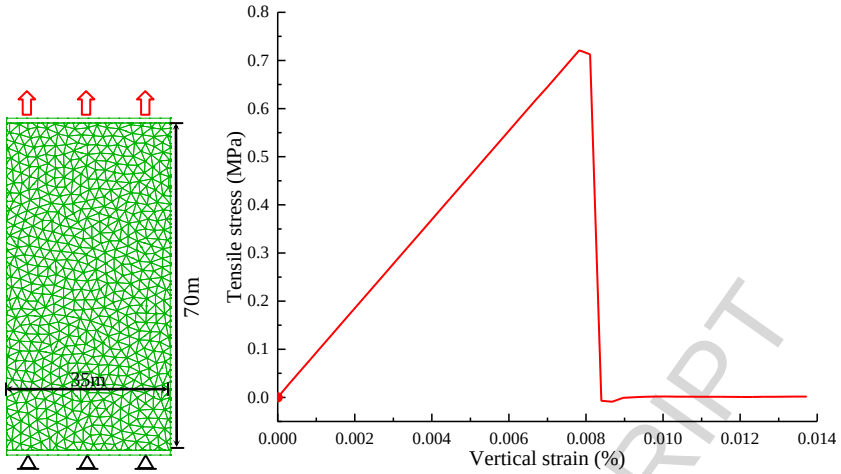

(a)

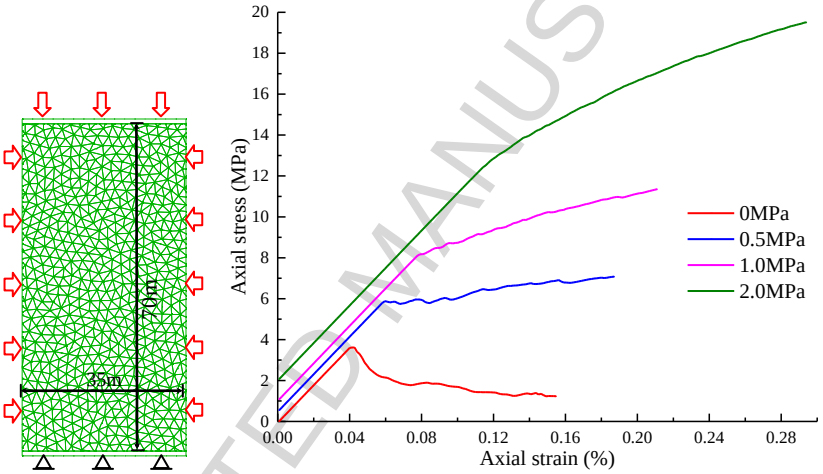

(b)

Fig. 7. Calibration of the UDEC trigon model. (a) The results of a direct tensile test showing the stress–strain curve obtained. (b) Axial stress–strain curves obtained from unconfined and confined compression tests (i.e. using confining pressures of 0, 0.5, 1.0, and 2.0 MPa).

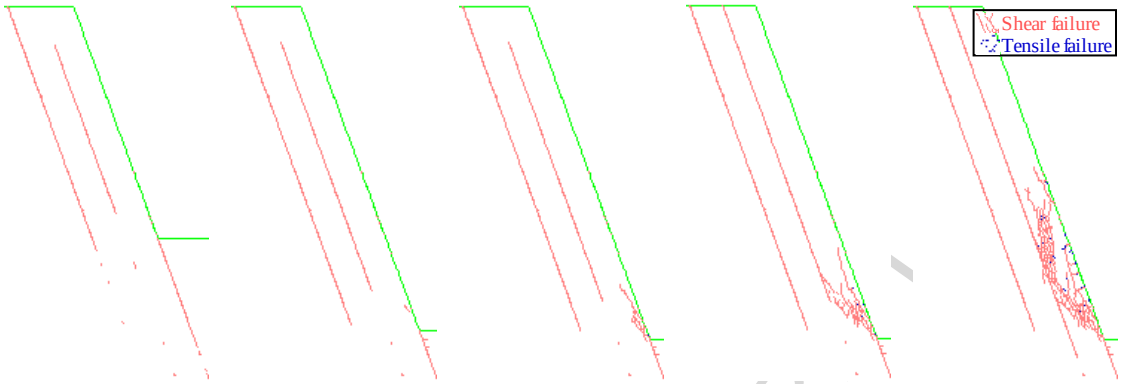

(a) 1 (b) 2 (c) 3 (d) 4 (e) 5

Fig. 8. The development of cracks during the downward excavation of the slope leading to slope failure. The five stages shown correspond to depths of: (a) 150 m, (b) 210 m, (c) 215 m, (d) 215 m, and (d) 215 m. Light red cracks denote shear failure; blue cracks tensile failure.

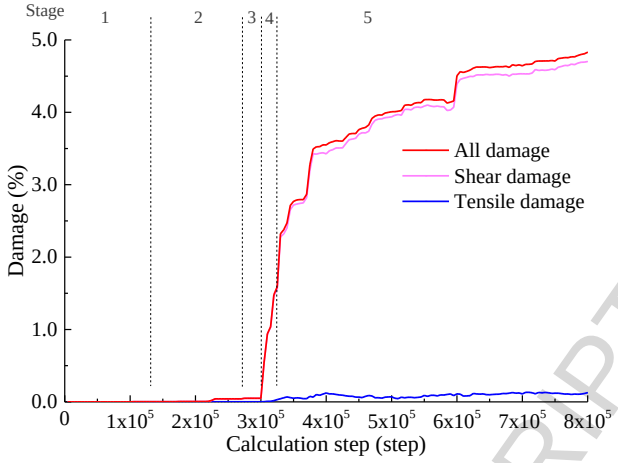

(a)

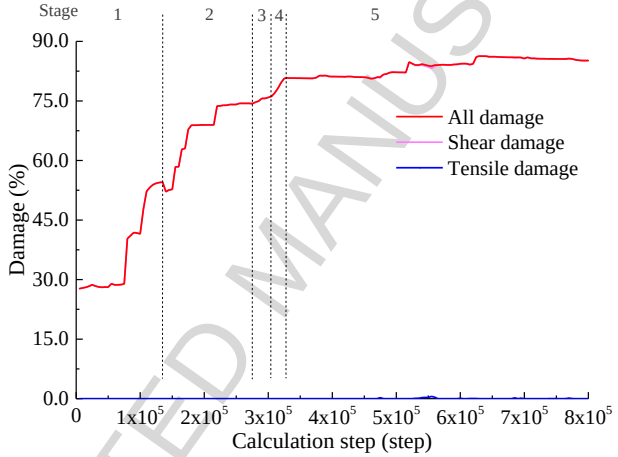

(b)

Fig. 9. Damage development during the failure process showing the damage in: (a) the intact rock, and (b) the persistent discontinuities.

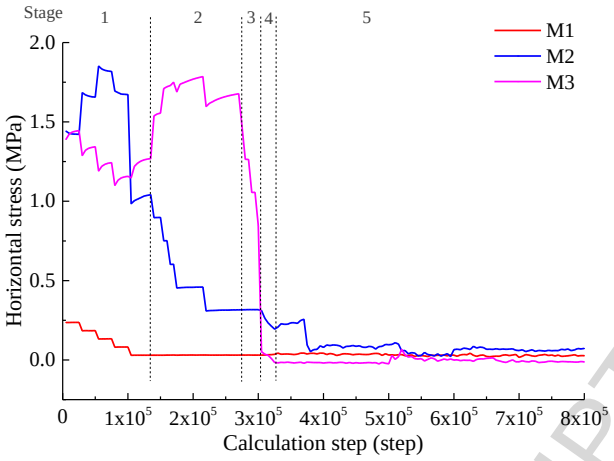

(a)

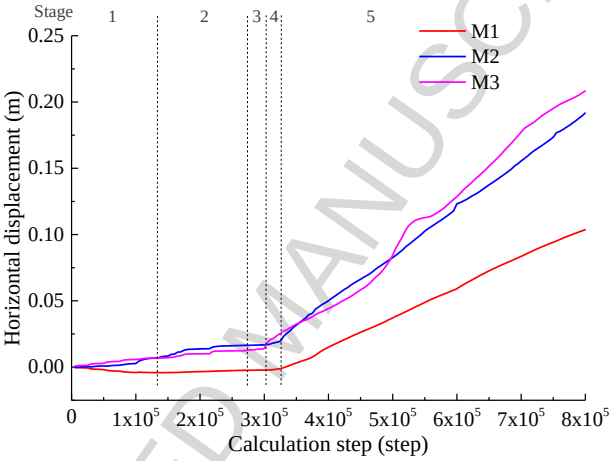

(b)

Fig. 10. Simulated monitoring data calculated for the points M1–M3 during excavation showing: (a) the horizontal stress experienced, and (b) the horizontal displacement of the monitoring points.

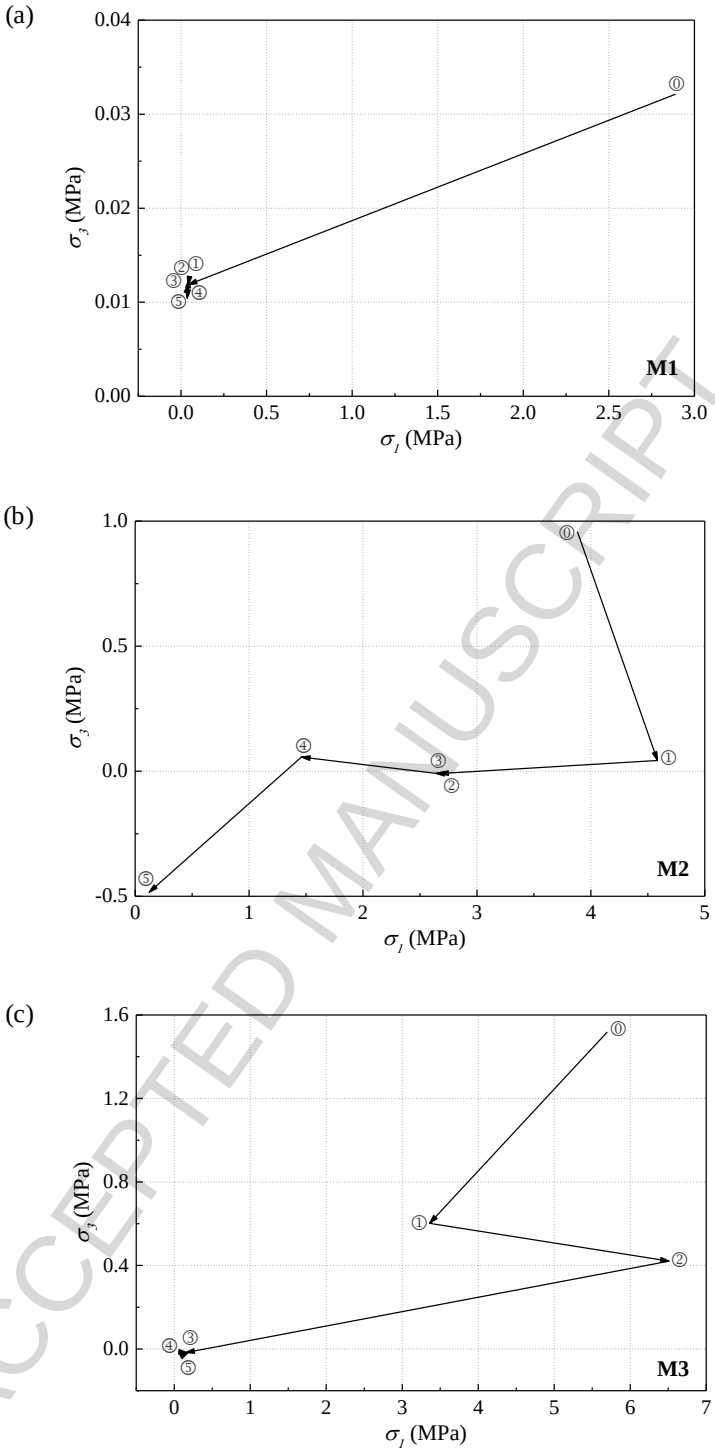

Fig. 11. Principal stress paths associated with five excavation stages for different zones showing: (a) M1, (b) M2, and (c) M3.

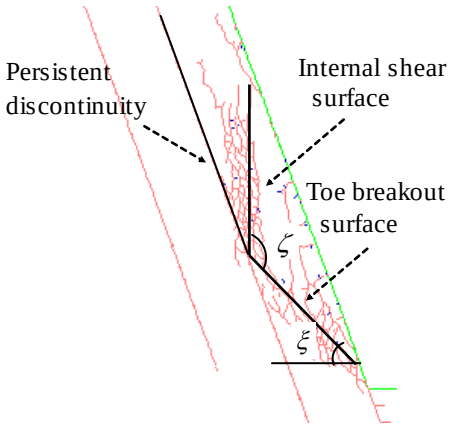

Fig. 12. The ultimate damage state of the footwall slope at the 225 m stage.

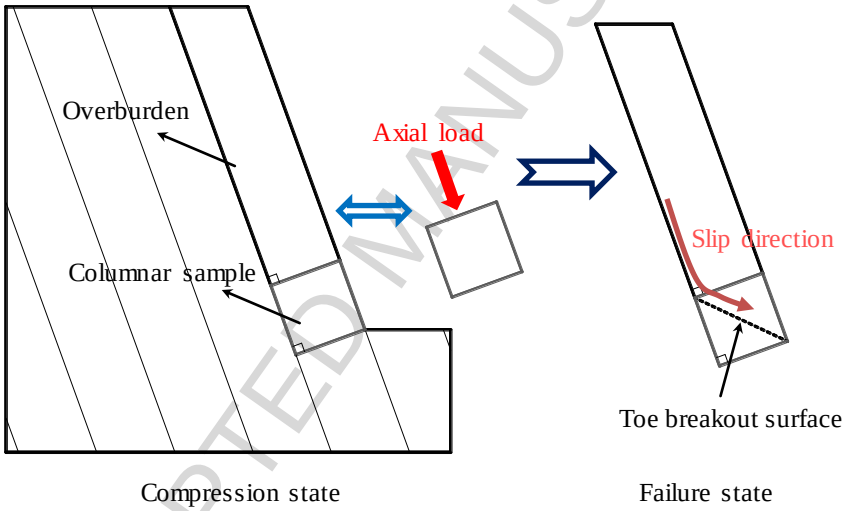

Fig. 13. Sketch map illustrating bi-planar footwall slope failure.

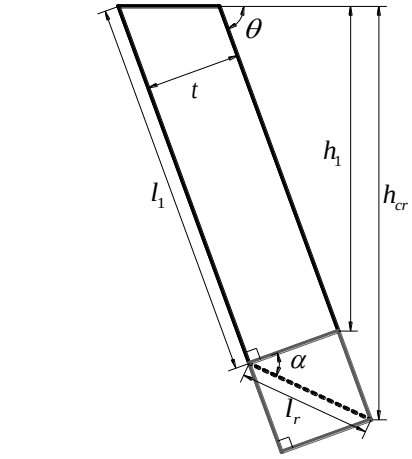

(a)

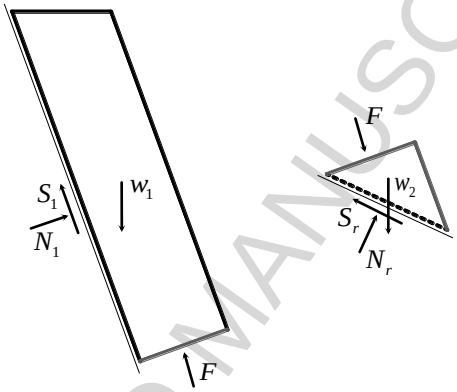

Overburden Columnar sample

(b)

Fig. 14. Schematic diagrams of models used to analyze the bi-planar failure process: (a) the geometric model, and (b) mechanical (force) model.

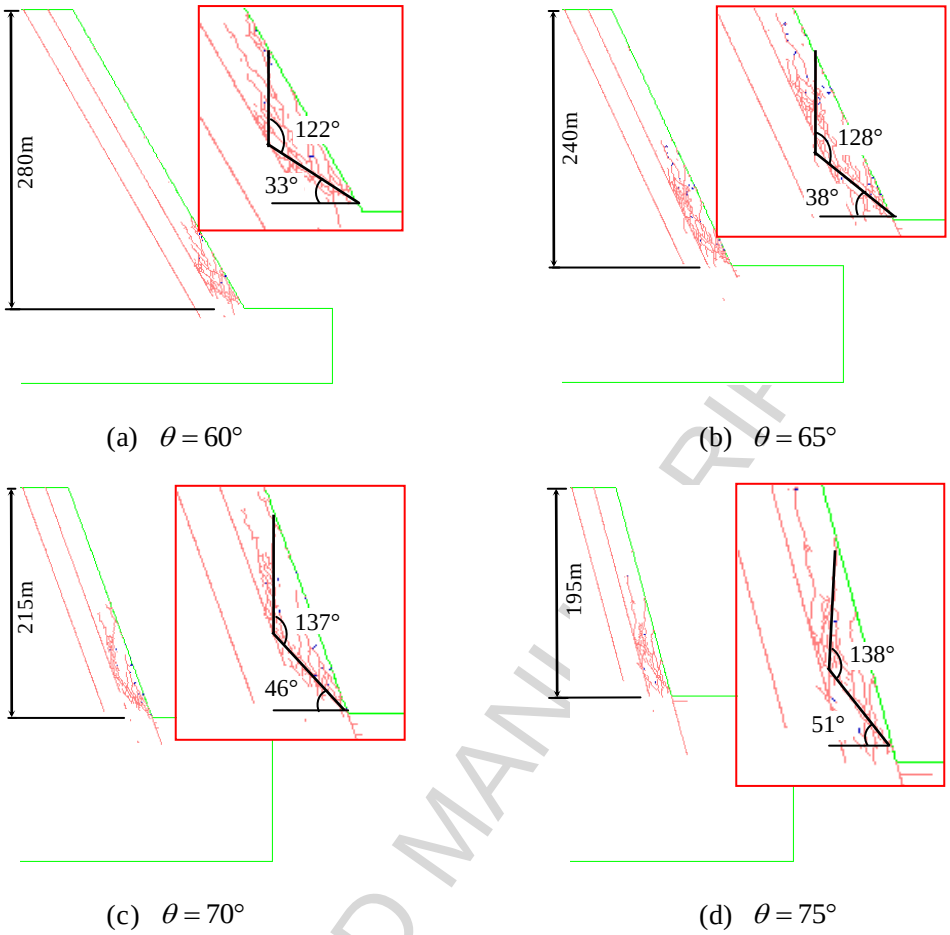

(a) $\theta = 60°$ (b) $\theta = 65°$

(c) $\theta = 70°$ (d) $\theta = 75°$

Fig. 15. Simulation results for bi-planar failure in slopes with different inclinations (θ values) showing the different values obtained for angles ξ and ζ.

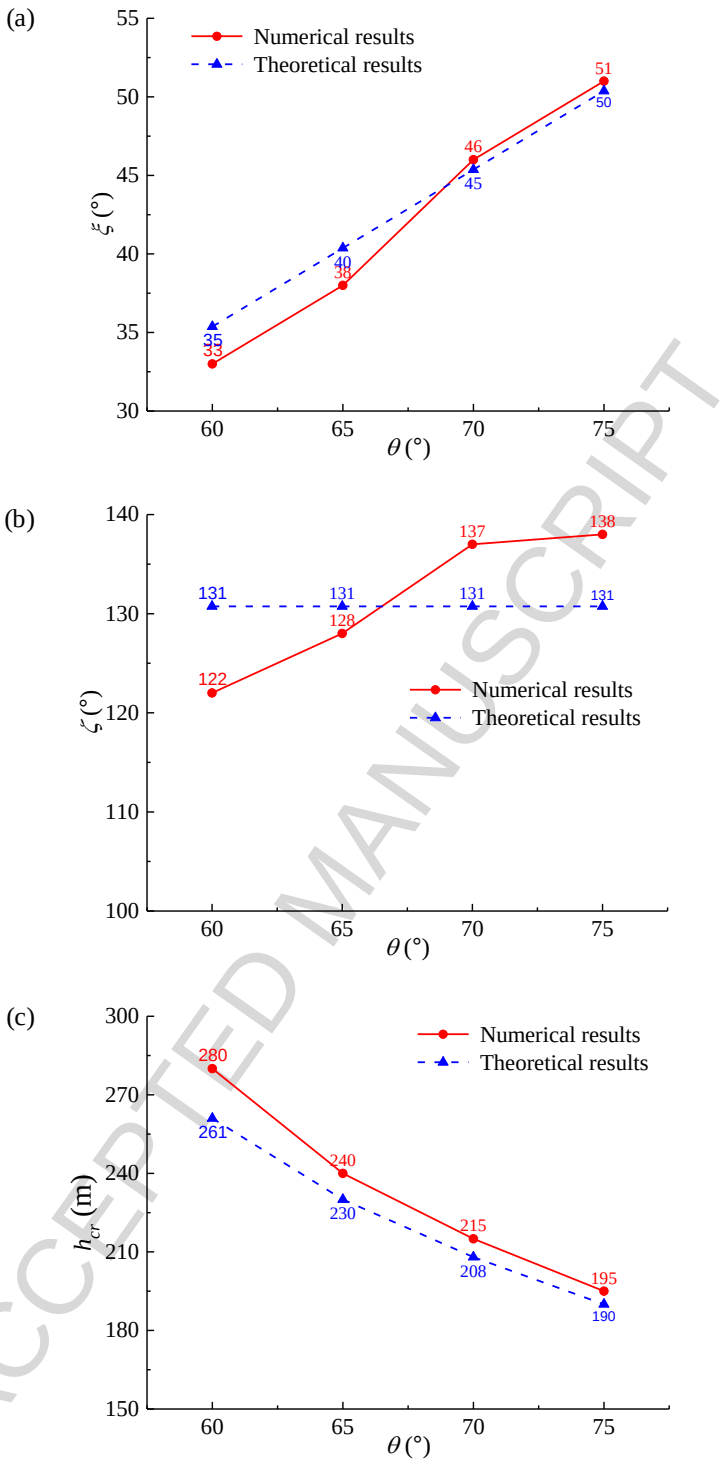

Fig. 16. Comparison of the results obtained for the different slopes using the theoretical method and numerical simulation showing the results obtained for: (a) the toe breakout angle (ξ), (b) the angle between the toe breakout and internal shear surfaces (ζ), and (c) the critical height (h_{cr}).

Tables

Table 1. The Hoek–Brown and Mohr–Coulomb parameters calculated for the rock mass.

Hoek–Brown parameters				Mohr–Coulomb parameters	
σ_{ci} (MPa)	GSI	m_i	D	c_r (MPa)	φ_r (°)
120	45	28	1	0.81	40.74

Table 2. The physical and mechanical properties of the rock mass.

γ (kN/m^3)	E_m (GPa)	μ	c_r (MPa)	φ_r (°)	σ_{tr} (MPa)
27	12.5	0.25	0.81	40.74	0.74

Table 3. The micro-parameters used in the UDEC trigon model.

Trigon block size (m)	Block properties			Contact properties				
	γ (kN/m^3)	K (GPa)	G (GPa)	k_n (GPa/m)	k_s (GPa/m)	c_j (MPa)	φ_j (°)	σ_{tj} (MPa)
2	27	8.33	5.00	33.33	13.33	1.28	40.90	1.00
3	27	8.33	5.00	22.22	8.89	1.28	40.90	1.00

Table 4. The parameters used for the persistent discontinuities.

k_n (GPa/m)	k_s (GPa/m)	c_j (MPa)	φ_j (°)	σ_{tj} (MPa)
4.44	1.78	0	35	0

Highlights

- Geological model of footwall slope is summarized based on the study of eleven diabase mines.
- Detailed process of bi-planar failure is captured using UDEC trigon approach.
- A new columnar mechanical model is proposed for bi-planar failure.
- Critical height of footwall slope can be determined using the columnar model.